IJCFD, 1997, Vol. 8, pp. 201–214
Reprints available directly from the publisher
Photocopying permitted by license only

Three-Dimensional Vortex Dynamics in a Shear-Driven Rectangular Cavity

T. P. CHIANG[a], W. H. SHEU[a] and R. R. HWANG[b]

[a]*Department of Naval Architecture and Ocean Engineering, National Taiwan University, 73 Chou-Shan Rd. Taipei, Taiwan, Republic of China;*
[b]*Institute of Physics, Academia Sinica, Taipei, Taiwan, R.O.C.*

(Received 10 November 1995; In final form 10 October 1996)

We investigate the vortical flow structure which has evolved in a rectangular cavity defined by a depth-to-width aspect ratio of 1:1 and a span-to-width aspect ratio of 3:1. The vortical system of interest consists of a dominant eddy, secondary motions, and spiraling spanwise motion. The objective of this study was to broaden knowledge of: 1) how the Taylor-Görtler vortices emerge and modify the flow structure; 2) why the left vortex differs from its right counterpart in each unsymmetric pair of TGL vortices. Most importantly, the intent of this study is to discuss the formation of flow instabilities from the energy standpoint.

Keywords: Secondary motions, Taylor-Görtler vortices, instabilities

1. INTRODUCTION

Computer simulation of fluid flows has received little attention for some time because many obstacles remain for its use in practical applications. Chief among them is the need to solve large systems of linear equations. Only recently, with the advent of computers exhibiting both fast processing speed and large storage capabilities, has the use of computational fluid dynamics (CFD) as a substitute for much more expensive experiments increased. The most notable attribute of CFD is that it is suitable for conducting parametric studies and exploring flow physics which are experimentally intractable. It offers significant potential for exploring in depth flow evolution by using a Navier-Stokes analysis code.

Lid-driven flow, resulting from an upper lid motion, represents a suitable benchmark for incompressible CFD codes and has been widely chosen for study. Its popularity is mainly attributable to its geometrical simplicity, which facilitates implementation of numerical analysis. This problem, as depicted in Figure 1, is also experimentally important since flow characteristics typical of industrial manufacture processes such as boundary layers, eddies of different sizes and characters, and various instabilities coexist in this cavity. As a result, experimental or predictive data are useful for gathering information about industrial flows.

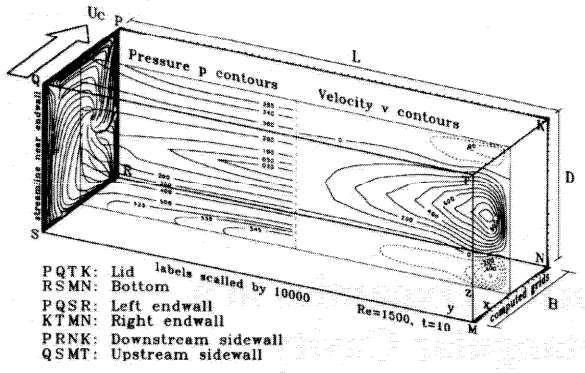

FIGURE 1 An illustration of investigated rectangular cavity, together with the computed pressure gradient, spanwise velocity, and end wall effect.

Investigation of the lid-driven cavity problem dates back to the pioneer work of Burgraff [1], which was followed by many two-dimensional analyses. While these studies shed light on some principal flow characters prevailing in the cavity, physical subtleties are still inaccessible because realistic flows are three-dimensional in nature. More recently, fueled by technological advances in computer hardware, the use of three-dimensional numerical simulation as a tool for investigating more realistic flow phenomena has been growing steadily. In a parallel development, experimental calibrations on the shear-driven cavity flow appeared in the early 1980s. An extensive literature review on the lid-driven cavity flow problem, experimentally or numerically, should include the work of Street and his colleagues [2–13]. In fact, experimental visualization and numerical prediction of Taylor-Görtler-like (TGL) vortices were reportedly found at Stanford University by Koseff *et al.* [3] and Freitas *et al.* [10], respectively.

Experimental investigation of cavity flows for Reynolds numbers between 1000 and 10000 started in the early 1980s. From 1982 to 1984, Koseff and Street [2–7] addressed the values of SAR ($\equiv$ L: B) on 1, 2, and 3. They observed not only the corner vortices in the vicinity of the two vertical end walls, but also the local TGL vortices. In the case of $Re \sim 3000$, eight pairs of TGL vortices were observed. At $Re \sim 6000$, three more pairs (11 pairs) of TGL vortices became visible. For Reynolds numbers as high as $6000 \sim 8000$, regular unsteadiness no longer remained and, thus, evolved into turbulence. Spiraling motion along the spanwise direction has been discussed mainly inside the downstream secondary eddy (DSE). In 1988–1989, Reynolds numbers falling into the range of $3200 \sim 10000$ were considered by Prasad, Perng and Koseff [8] and Prasad and Koseff [9], who took different values of SAR = 1:2, 2:3, 5:6, and 1:1 into consideration. The emphasis of their study was placed on investigating the influence of the reduced SAR on the increase of viscous drag originating from the two end walls. More recently, Reynolds numbers classified as low to medium ($100 \sim 2000$) were considered by Aidun *et al.* [14] Their paper is important in that they provided a detailed description of how the flow characteristics vary with Reynolds numbers.

In 1991, the GAMM-Committee sponsored a workshop dedicated to numerical simulation of a lid-driven cavity flow at $Re = 3200$ for SAR = 3:1. To provide some insight into the computed results, Deville Lê and Morchoisne [15] summarized and discussed the main features of the solutions obtained by the contributors of this workshop. Comparison studies were made on the number of TGL vortex pairs appearing in the transverse direction, on the performance of the computed codes employed, and on the CPU time per unit of physical time. It was surprising to find that the conclusions were quite different among the contributors not only on the accessibility of flow symmetry, but also on the number of pairs of TGL vortices. In recognition of this, we feel that much work needs to be done in the years ahead. As a result, we consider a Reynolds number much lower than 3200. For numerical simulations of a cavity flow at Reynolds numbers other than 3200, the reader is referred to Deng *et al.* [16]

We begin by introducing the equations of fluid motion for the incompressible case in Section 2. Subsequently, the underlying finite volume discretization method, together with the solution algorithm and the multi-dimensional advection

scheme, are briefly described. In Section 3, we validate the applicability of the computer code by carrying out an intensive comparison with analytic results. In Section 4, we discuss in detail the complex flow, which is rich in interesting phenomena, from different viewpoints. Numerical tests in this section bear out the presence of TGL vortices. Attention is given to a physical explanation of the onset of laminar instability from the energy viewpoint and the transport kinetics of TGL vortices. Closing remarks are presented in Section 5.

2. MATHEMATICAL AND NUMERICAL METHOD

The mathematical model, permitting analysis of incompressible and viscous fluid flows, takes the following form for a given Reynolds number *Re*:

$$\frac{\partial u_i}{\partial x_i} = 0, \tag{1}$$

$$\frac{\partial u_i}{\partial t} + \frac{\partial}{\partial x_m}(u_m u_i) = -\frac{\partial p}{\partial x_i} + \frac{1}{Re}\frac{\partial^2 u_i}{\partial x_m \partial x_m}. \tag{2}$$

In the open literature, we find several sets of working variables to choose from. Amongst these alternatives, we abandon others in favor of the primitive-variable formulation mainly because this setting accommodates the closure boundary and initial conditions [17].

Two fundamental impediments to application of equations $(1 \sim 2)$ in modelling incompressible Navier-Stokes equations are briefly described below. The first deals with the stability problem when a problem of advection dominance is considered. Very often, numerical prediction error suffers from oscillatory velocities and false diffusion errors, grossly polluting the flow physics over the entire domain. In order to alleviate these difficulties, we advocate the use of the third-order upwind QUICK [18] scheme to model nonlinear advective fluxes defined in a non-uniformly discretized domain. The reader is referred to reference [19] for additional details. The remaining diffusive fluxes and pressure gradient terms, are, as usual, discretized by second-order centered schemes. A fully implicit forward time integration scheme is used for the time derivatives. Moreover, discretization errors stemming from the use of a one-to-one curvilinear coordinate transformation are considerable provided the problem of interest involves complex geometry and highly distorted meshes. Because there is potential loss of accuracy arising from the calculation of metric tensors, to accurately explore the rich physics, we conduct analysis of a cavity containing rectangular grids.

In as much as the velocity-pressure formulation is considered, we are faced with the choice of grid staggering [20] or collocating [21] strategies to store these working variables. While numerical instabilities exhibiting node-to-node pressure oscillations can be suppressed at both grids, we favor the staggered grid setting and exploit it to get rid of these oscillatory pressures regardless of programming complications. We abandon collocating grids due to a lack of the closure boundary pressure, which is indispensable for an analysis involving a Poisson-type pressure correction equation. On the control surface of a finite volume cell, each primitive variable takes over a node to itself whereas the pressure node is surrounded by its adjacent velocity nodes. This permits natural use of finite volume integration for each working differential equation under these circumstances.

Even though the discrete divergence-free velocities can be unconditionally ensured by using a mixed formulation, we encounter a much larger discrete system. The need to resolve the demand for much larger computer storage has prompted researchers to consider segregated approaches. In the present paper, the solutions to the finite volume discretization equations are obtained sequentially for all primitive variables using the underlying SIMPLE iterative algorithm [20].

3. VALIDATION STUDY

As a means of conducting investigation of vortical flow in a cavity, we first validate the computer code by means of an analytic problem. In an attempt to verify the flux discretization scheme as applied in the present analysis tool and to then estimate its spatial rate of convergence, we consider the Navier-Stokes problem of Ethier and Steinman [22]. In a simple domain of three dimensions $(-1 \leqslant x, y, z \leqslant 1)$, the solution to equation $(1 \sim 2)$ takes with $Re = 1$ the following analytic form:

$$u = -a[e^{ax}\sin(ay \pm dz) + e^{az}\cos(ax \pm dy)]e^{-d^2t},$$

$$v = -a[e^{ay}\sin(az \pm dx) + e^{ax}\cos(ay \pm dz)]e^{-d^2t},$$

$$w = -a[e^{az}\sin(ax \pm dy) + e^{ay}\cos(az \pm dx)]e^{-d^2t},$$

$$p = -\frac{a^2}{2}[e^{2ax} + e^{2ay} + e^{2az}$$

$$+ 2\sin(ax \pm dy)\cos(az \pm dx)e^{a(y+z)}$$

$$+ 2\sin(ay \pm dz)\cos(ax \pm dy)e^{a(z+x)}$$

$$+ 2\sin(az \pm dx)\cos(ay \pm dz)e^{a(x+y)}]e^{-2d^2t},$$

where $a = \frac{d}{2} = \frac{\pi}{4}$. As is usual, we assess the quality of the finite volume solutions on the basis of nodal values computed in the uniformly discretized domain. We measure the discretization error by calculating the difference between the finite-volume solutions and the analytic solutions. With these nodal errors being computed, we sum them to yield an L_2-error norm. With grid spacings continuously refined, we can compute the rate of convergence.

We have carried out computations at a time spacing $\Delta t = 1/160$ and under several grid spacings ($h = 1, 2/3, 1/2, 2/5, 1/3, 2/7$). According to the finite volume solutions at $t = 0.1$, the good agreement demonstrated in Figure 2 confirms the applicability of the proposed scheme to analyzing incompressible Navier-Stokes equations. The results of this analytic validation study encourage us to proceed with investigation of the flow physics which are driven by a constant upper lid in a rectangular cavity.

4. RESULTS AND DISCUSSIONS

In this section, we will describe the simulation of a three-dimensional incompressible fluid flow inside a rectangular cavity, as defined by L : B : D = 3 : 1 : 1 in Figure 1. The Reynolds number chosen for this cavity is based on the lid speed, the width of the cavity, and the kinematic viscosity of the working fluid. At time $t = 0$, the roof of the cavity of the present interest is driven by a sudden lid motion. Experimental evidence [14] reveals TGL vortices become visible at Reynolds number beyond 1300. These laminar instabilities continue to evolve into turbulence at $Re = 6000$. With this recognition, we deal only with Reynolds numbers whose values are not so high as to render a turbulent flow simply because of the complication of turbulence modeling. On the other hand, the

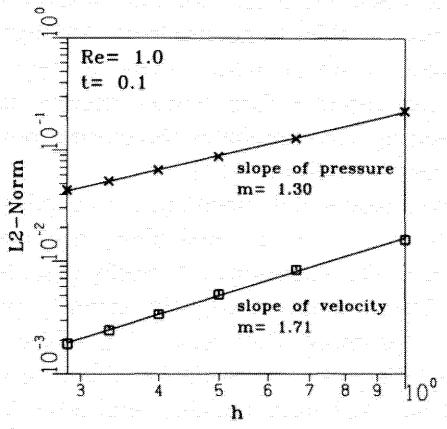

FIGURE 2 The computed rates of convergence for velocities and pressure based on the Navier-Stokes equations define in a cubic.

Reynolds numbers considered must not be too small (less than 1300); otherwise, the TGL vortices will not emerge in the confined cavity. Physical as well as computational reasoning leads us to conduct analysis at a moderate Reynolds number $Re = 1500$. To avoid ambiguity regarding whether or not symmetry of the flow will persist in the investigated rectangular cavity, we simulate the flow physics in the whole cavity having non-uniform grids of $34 \times 91 \times 34$ resolution. For each time step in this three-dimensional analysis, the disk space required is roughly 1.8 M bytes while for the core memory it is about 6 Mbytes. Normally, ten days of CPU time, as measured on an HP730, are needed to complete a calculation involving a time evolution of 450 seconds.

As noted in the introduction, the flow of a viscous fluid in a three dimensional cavity driven constantly by a sliding upper plane has been extensively studied because of its geometric simplicity and well defined flow structure. As a result, we consider spanwise ratio SAR = 1, and Reynolds numbers 400 and 1000, for further confirmation of whether the computer code being analytically verified is applicable to simulation of this problem. The simulation quality was assessed on the basis of mid-sectional velocity profiles along both the vertical and horizontal centerlines. According to the computed finite volume solutions and grid refinement tests, as depicted in Figures 3(a, b), for the cavities considered and the Reynolds numbers investigated, the agreement with other numerical solutions [23–26] is close enough. In the remaining sections, we will focus on subjects which have been little explored. To shed light on the onset of TGL vortices from the energy viewpoint, we have computed the kinetic energy from the computed primitive working variables.

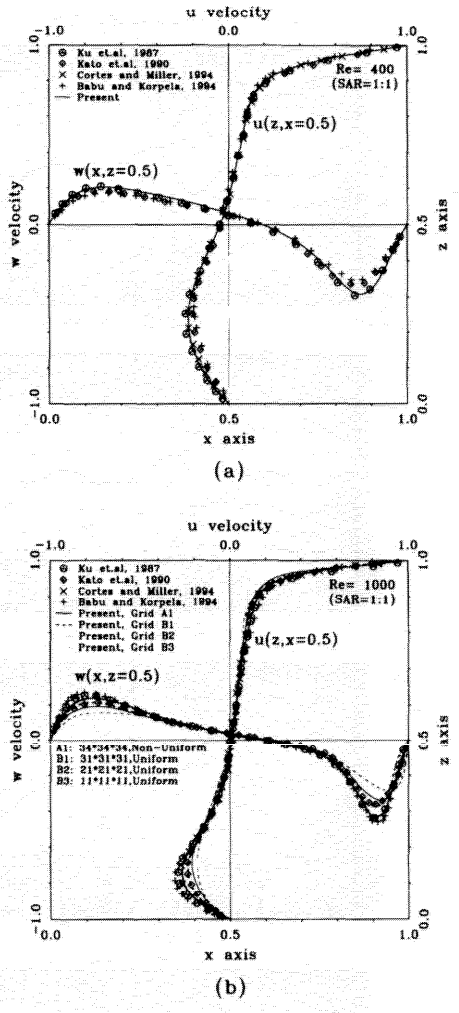

FIGURE 3 Comparison study of mid-sectional velocities at the symmetry plane $y = 0.5$ for SAR = 1. (a) $Re = 400$; (b) $Re = 1000$.

4.1. Dynamics of TGL Vortices

From pioneer work using experimental observation [3] and numerical prediction of TGL vortices [10], we realize that in high Reynolds number circumstances, the incompressible system in a rectangular lid-driven cavity can support TGL vortices. The question remains unanswered whether TGL vortices are still present at a much lower Reynolds number, say $Re = 1500$. We plot the velocity distributions along the spanwise direction. Of these wavy velocity profiles, the crest of u in Figure 4 corresponds to the trough of the velocity profile w. The spatial location where the spanwise velocity experiences an inflection is exactly where the local extremities of u and w are located. Velocity profiles characterized as possessing

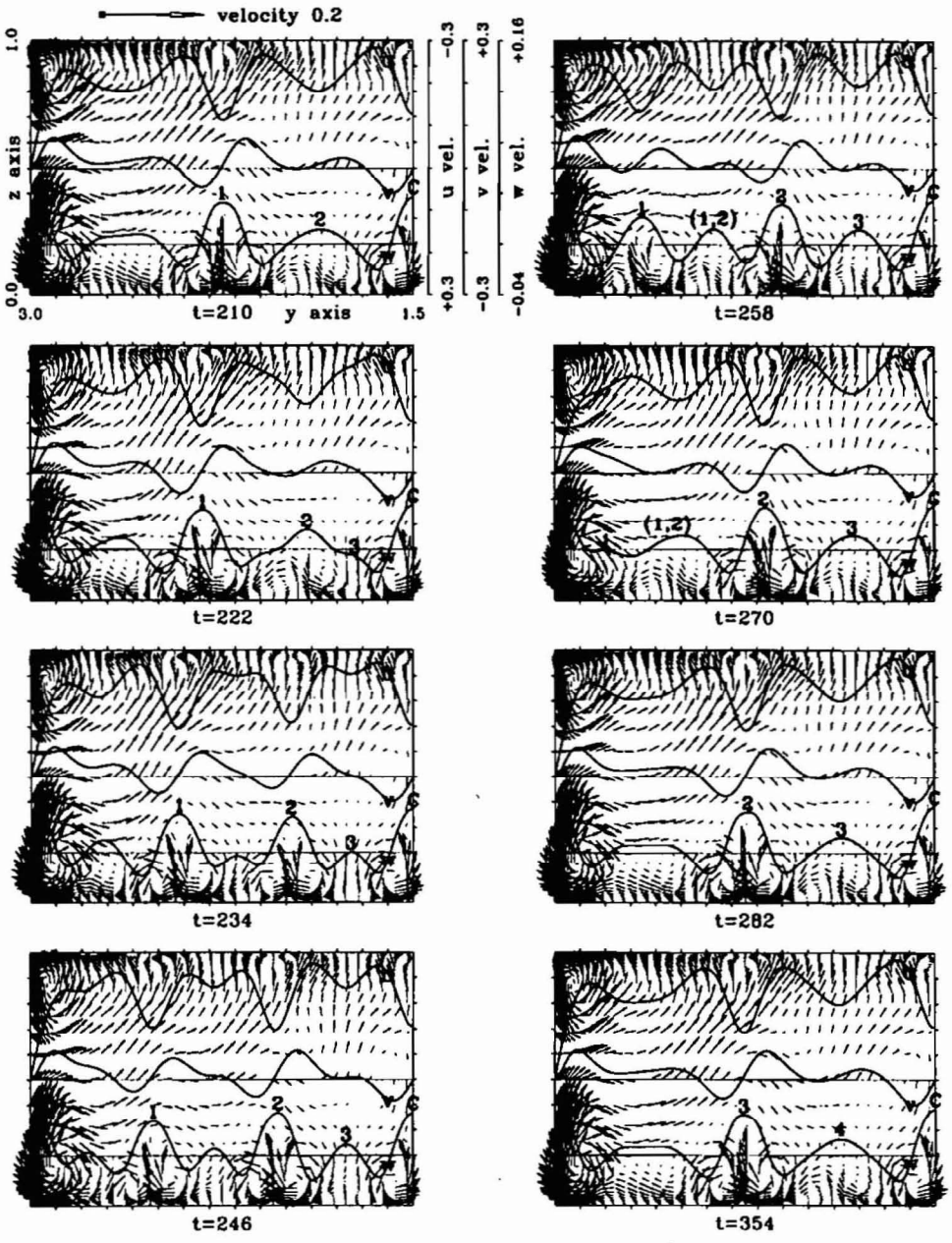

FIGURE 4 Computed solutions plotted at the plane $x = 0.525$.

coexistence of maximum, minimum, and inflection at the same location have a strong resemblance to the longitudinal Taylor-Görtler vortices which were originally found in the concave boundary layer. The name Taylor-Görtler-like (TGL) vortices stems from this similarity. There is some analogy between the centrifugal force in the concave boundary layer and the buoyancy force in the thermal stratification layer. In many industrial flows, Taylor and Rayleigh instabilities may coexist.

These vortices might interact with each other, leading to premature transition to turbulence, and thus aid the transfer rate.

Due to space considerations, we will address in this paper only the kinetics of Taylor-Görtler vortices at a time beyond the periodic motion. The plausible causes leading to the formation of TGL vortices have been clearly discussed in our previous work [19]. Subsequent to $t = 138$, Taylor Görtler vortices evolve into a periodic motion. To confirm that periodicity is indeed attainable, we have plotted TGL vortices from $t = 210$ to $t = 354$ in Figure 4, from which we find that the time period is 72. TGL vortices emanating from a spanwise location fall into the domain between the symmetry plane and its adjacent vortices. They proceed along the same direction as do the nearby TGL vortices that will be immersed to the corner vortex. As a result, no more than five pairs of TGL vortices are visible over the entire span. These possible well-established TGL vortices can be furthermore divided into two classes, depending on the nature of their symmetry. As seen in Figure 5, for TGL vortices established at the symmetry plane, $y = 1.5$, their physical symmetry can be well-maintained. In contrast, the remaining TGL vortices fail to retain symmetry. According to their formation mechanism, we classify the left vortex as being a well-shear vortex and the one on the right side as a free-shear vortex. At $t = 258$, TGL vortices (TGL(1, 2) in Fig. 4) emerge in between two well-developed TGL vortices, as designated by "1" and "2" in Figure 4. The nearer the end wall approaches, the larger the size of this pair of TGL vortices is. The flattened velocity profiles, as seen in Figure 4 at $t = 270$ and 282, are attributable to mutual interactions among the TGL vortices TGL(1, 2) and the left corner vortex.

In light of Figures 6 and 7, the time-periodicity is well-maintained at 72. As to the formation of TGL vortices at the symmetric location, the maximum value of w velocity varies in a mild and periodic fashion. This implies that the TGL vortices (TGL C) at the symmetry plane are fairly stationary. As for unsymmetric TGL vortices (TGL

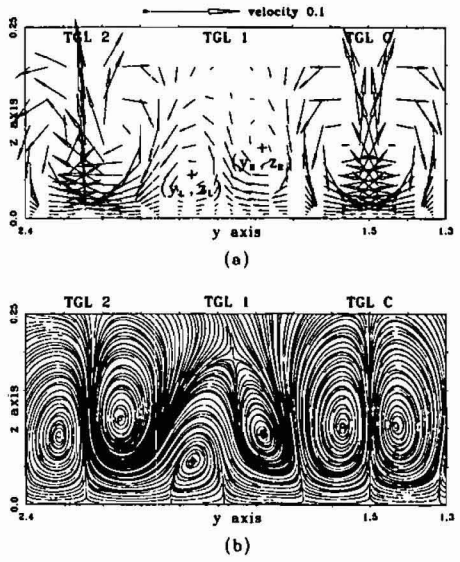

FIGURE 5 Finite volume solutions computed at $t = 138$ and $x = 0.525$ plane for showing the symmetry behavior of the TGL vortices (at the mid span $y = 1.5$) and the asymmetry of the rest of TGL vortices. (a) velocity vector plots; (b) streamlines.

1, 2, 3, 4), shown in Figure 7, an increase in w is clearly illustrated, followed by small-scale fluctuations. A rapid decrease in w is observed as the end-wall is approached. In circumstances when TGL vortices are immersed into the corner, another pair of TGL vortices emerges.

Physical reasoning suggests that the w profile, as shown in Figure 4, is best-suited to illuminating TGL vortices. We designate "3" at the spatial location $y \sim 1.7$ so as to facilitate demonstration of the formation of TGL vortices next to the symmetry plane. It takes a time period ($\Delta t = 72$) for marker "3". shown in Figure 4, to return to the location at which marker "2" is located. Similarly, another period of time is needed for marker "2" to proceed to the location marked by "1" in Figure 4. In the meantime, marker "1" continues its journey toward the end-wall. A period of time is in need before marker "1" is immersed into the corner eddy at $y \sim 2.8$. In summary, for TGL vortices just next to the symmetry plane, it takes three time periods for them to complete the entire transport process.

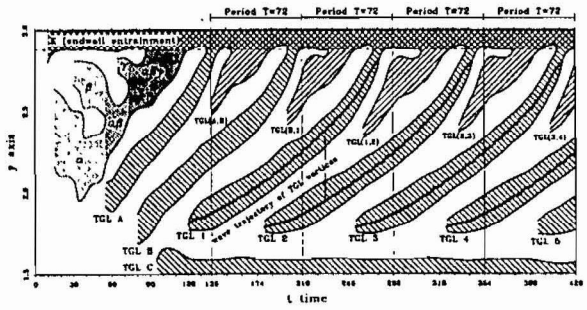

FIGURE 6 Description of the size of detached upstream separation surface, measured in y, for TGL vortices and corner eddy in the whole evolution.

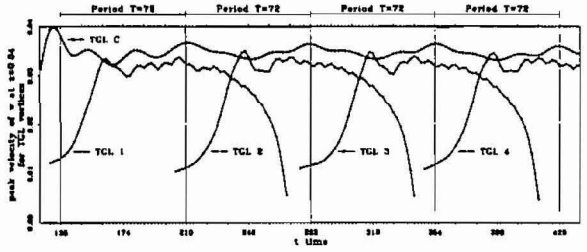

FIGURE 7 Time history plots for showing the maximum velocity component w, measured at $z = 0.04$, for different TGL vortices.

Within a time period of $\Delta t = 72$, we can divide the vortical system into four major groups. In Figure 4, over the entire span, there exist three well-developed pairs of TGL vortices at $t = 210$ which are roughly spaced with a constant length of 0.75. In between these developed TGL vortices, new TGL vortices tend to emerge. After a half time period or $\Delta t = 36$, five sets of mature TGL vortices become visible. While these vortices are symmetric with respect to the $y = 1.5$ plane, they are slightly unsymmetric within themselves, as seen in Figure 4 ($t = 246$). The magnitudes of w for three middle TGL vortices, equally displaced with a distance of 0.52, are almost identical to each other. For the remaining two pairs, they are distanced from the end wall with a length of 0.49. In between $t = 210$ and $t = 246$ and between $t = 246$ and $t = 282$, three to five pairs of well-developed TGL vortices can be observed. By taking the differentiation of the y coordinate at which w takes its local maximum with respect to time, we can obtain the corresponding wave speeds. From Figure 8, we realize that TGL vortices do not necessarily proceed monotonically along the spanwise direction. In fact, subsequent to $t = 138$, a highly rugged wave seems to last for one and half time periods for each three time periods.

In an attempt to clarify that asymmetry does exist in the TGL vortices, we consider one pair of vortices of this kind nearby the symmetry plane. We designate (y_L, z_L) and (y_R, z_R) as the rotational centers for each of the counter rotating vortices, shown in Figure 5. The values of y_L and y_R plotted in Figure 9(a) reveal that vortices of different

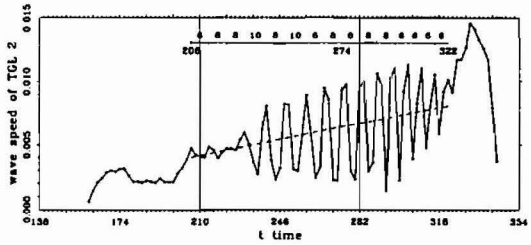

FIGURE 8 A plot is showing the transport velocity of TGL 2.

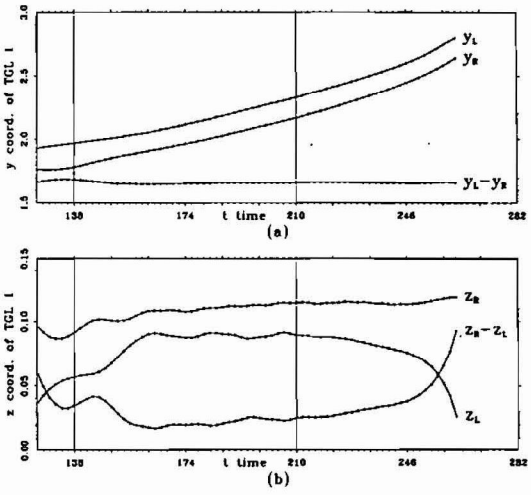

FIGURE 9 Vortex centers (defined in Fig. 5) for a unsymmetric pairs of TGL vortices (a) A plot in showing the distance, in the spanwise direction, between two vortices which constitute a pair of unsymmetric TGL vortices. (b) A plot in showing the asymmetry of TGL vortices against time.

physical relevances proceed with a fairly equal spanwise velocity. From the plot depicting the evolution of the heights of two rotationary centers, a large discrepancy is clearly visible in Figure 9(b). Within $138 \leqslant t \leqslant 282$, the values of z_R and z_L continue to increase until $t = 162$. Prior to $t = 210$, two vortices are equally displaced along the z direction. Subsequent to this time, z_R maintains a slowly increasing pace while the pace of z_L drops sharply. This results in a marked change in their relative positions in the vicinity of the two end walls. The main cause of this difference is the rotational velocity direction. Of the two vortices, the rotation direction of the TGL vortex adjacent to the corner is opposite to that of the corner vortex. The velocity is thus cancelled out by the corner vortex so that the strength of the wall-shear induced TGL vortices tends to be smeared by the corner vortex. Unlike the wall-shear induced vortex, the free-shear induced vortex is only slightly affected because it rotates in the same direction as does the corner vortex.

The revealed counter-rotating TGL vortices have close resemblance in their velocity components. It is, thus, worthwhile to look for plausible reasons why four of the five sets of TGL vortices are unsymmetric. To elucidate the origin of this asymmetry, we have plotted in Figures 10(a, b, c) the streamlines at planes $x = 0.525$, $z = 0.525$ and in Figure 11 the so-called USE cut plane. In the very early stage, say $t = 15$, the corner vortex becomes clearly visible even though the contour line of $v = 0$ varies little in regions away from the end wall. After a time interval of $\Delta t = 10$, a circulation cell is established as a mutual consequence of the developing corner vortex and the outward-running spiraling flow motion over the bottom plane. This circulation cell interacts with the corner vortex at spatial locations near the two end walls. This cell will be engulfed in the corner and will, thus, enhance the corner vortex at $t = 65$, followed by a newly developing circulation cell of the same physical character. Subsequent to $t = 70$, this cell grows in size and interacts with the corner vortex. Before being engulfed into the corner vortex, another circulation cell is established. As clearly evidenced from the wavy contour line of $v = 0$ shown in Figure 10, the first roller of primary flow relevance is established at $t \sim 75$. In between the two circulation cells which are away from the bottom wall, a circulation cell emerges from the boundary layer. Then, in between the two counter-rotating vortices originating from different physical relevances, the separated boundary layer is clearly manifested by upward velocities. Notable in Figure 10, is that the isoline of $v = 0$ crosses these counter-rotating vortices. Taking into consideration a control volume of small size, over which the interface of these vortices is located and the spanwise velocity is negligibly small, the velocity component in the direction of the lid-plane motion decreases due to the underlying conservation of energy. The velocity distribution, thus, tends to be of the Görtler type. Exclusive of the TGL vortices located at the symmetry plane, $y = 1.5$, the right vortex in each pair of TGL vortices is classified as the free-shear vortex while the left one is the wall-shear vortex. Clear demonstration of the asymmetry of two vortices can be found in Figure 5. According to Figure 10, the formation of one shear-induced circulation cell at $t = 85$ and another circulation cell emanating differently from the primary region paves the way for the emergence of another new pair of TGL vortices.

During the course of the formation of TGL vortices, we measured the height and width for both secondary eddies. We have summarized them graphically in Figure 12. As the separation surface at the upstream side detaches from the vertical side wall, the width of the USE tends to increase. The summit forms accordingly. In contrast, the valley forms in regions where the width of the DSE decreases. Once the vortex pairs reach the local maximum kinetic energy, at time $t = 85$ for example, the USE width and DSE width shown in Figure 12(a) evolve to their extreme values. At that moment the spanwise length of "A", shown in Figure 12(a), is exactly the length of two spatial points where the line of USE width intersects with

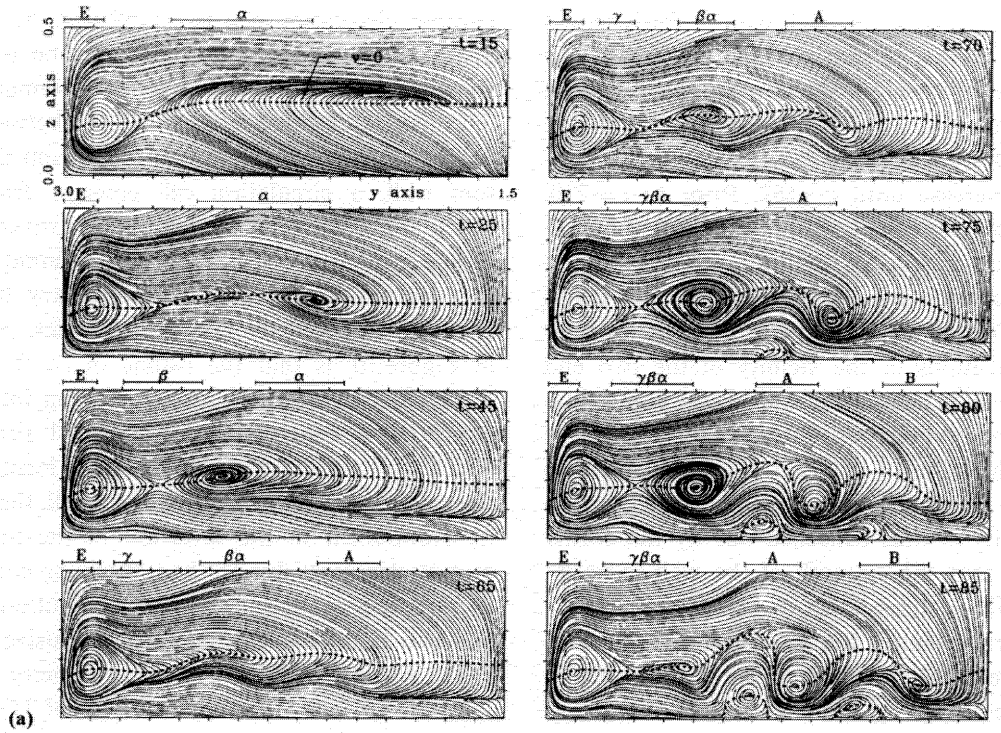

(a)

FIGURE 10 Computed solutions plotted in terms of streamlines for showing how TGL vortices form. (a) at $x = 0.525$ plane; (b) at $z = 0.525$ plane; (c) at USE cut plane (defined in Fig. 11).

the line of DSE width. To confirm that this finding is universal to the investigated lid-driven cavity, we have plotted widths and heights for both secondary eddies. Plots depicted in Figures 12(b,c) not only confirm the above conclusion, but also provide us with a clear illustration of the flow periodicity for $\Delta t = 72$. Figure 6 plots the length of the upstream detached separation surface against the time frame. This figure provides another viewpoint for understanding the evolution of the formation-transport-termination of TGL vortices (designated by A, B, C, 1, 2, 3, 4, 5). In the whole evolution period of $\Delta t = 426$, the symmetric TGL vortices (TGL C) which formed at $y = 1.5$ do not emerge until $t = 95$. Once this pair of TGL vortices forms, it remains quite stationary. This figure also clearly shows the formation of new TGL vortices, as designated by TGL(A, B), TGL(1, 2) etc.

4.2. Energy Aspect in Association with the Formation of TGL Vortices

We will now discuss the formation of TGL vortices, or the onset of laminar instabilities, from the energy viewpoint. In the present incompressible and isothermal flow system, the specific total energy varies only with the potential and kinetic energy. In particular, the kinetic energy represents the primary change of the total energy because the potential energy in the investigated system varies very little. In response to a disturbance, the underlying energy principle dictates that the fluid flow remain in a minimal energy status if the system still remains stable. This clearly explains the necessity of plotting energy contour levels in the vicinity of the maximal kinetic energy to determine where TGL vortices will most likely develop.

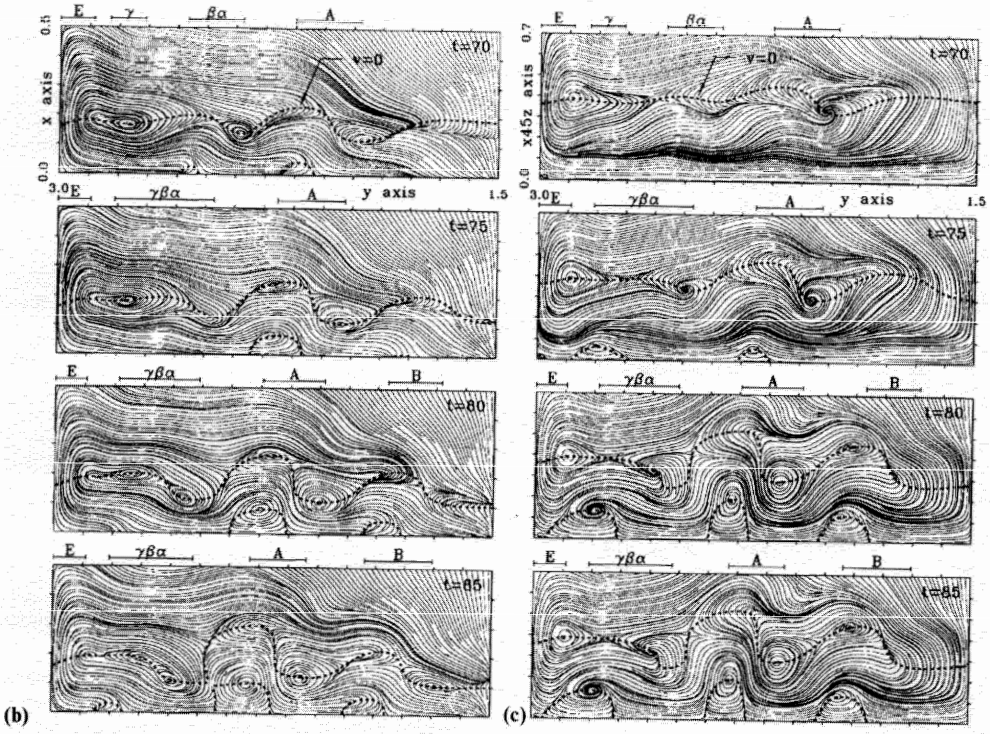

FIGURE 10 (Continued).

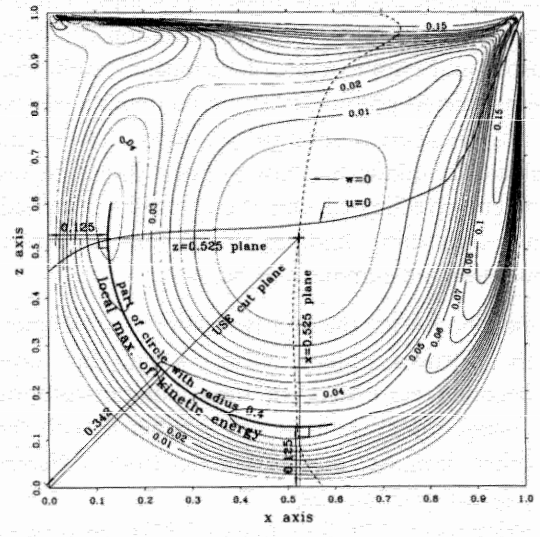

FIGURE 11 Contour plots of kinetic energy at the symmetry plane $y = 1.5$ and at time $t = 25$ for indicating where the local maximum kinetic energy locates.

Figure 13 shows the kinetic energy $\frac{1}{2}(u^2 + v^2 + w^2)$ at the plane $x = 0.525$. From this figure, it is surprising to find that the location where the free-shear roller is located always falls into the highest level of kinetic energy, as denoted by the dotted regime. This shows that the occurrence of TGL vortices is closely related to the larger kinetic energy.

Now, it is worthwhile to explain why we are interested in plotting figures at the $x = z = 0.525$ planes. The main reason is that the structure of TGL vortices can be most clearly seen there. At a spanwise location $y = 1.5$, we have plotted the contour lines of kinetic energy at time $t = 25$ in Figure 11. This figure clearly shows that the local maximal of kinetic energy falls into a part of a circle, centered at $(x = 0.525,\ z = 0.525)$ with a radius of 0.4. This implies that as TGL vortices emerge, they will most likely appear and be clearly visualized in a plane cutting through $(x = 0.525,\ z = 0.525)$ where the kinetic energy takes on its local

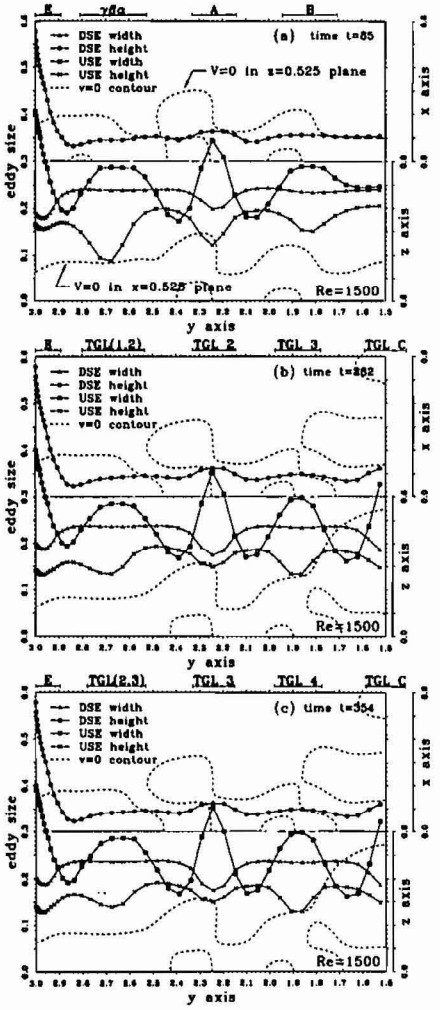

FIGURE 12 Illustration of width and height of secondary eddies together with the contour lines of zero spanwise velocity at $x = 0.525$ and $z = 0.525$ planes, against the coordinate y. (a) $t = 85$; (b) $t = 282$; (c) $t = 354$.

maximum value. Finally, we have plotted in Figure 13 the contours of kinetic energy at the $x = 0.525$ plane to illustrate the relationship between the local maximal kinetic energy, the detached upstream separation surface, the TGL vortices, and the zero contour lines of spanwise velocity.

5. CONCLUDING REMARKS

In this paper we have applied a QUICK-type advective scheme and a finite volume method to explore

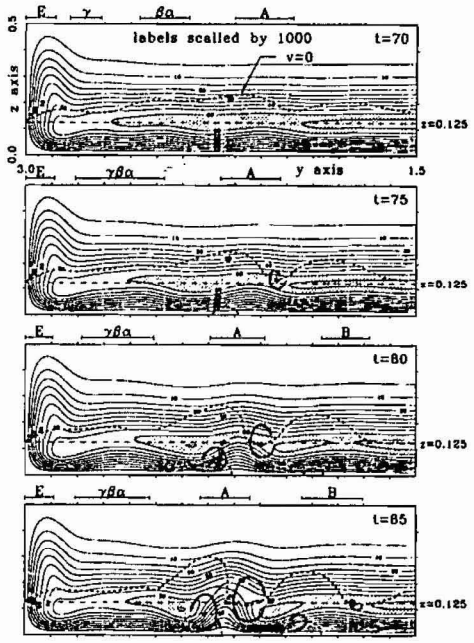

FIGURE 13 Computed plots at $x = 0.525$ plane for showing the formation of TGL vortices from the energy principle. The shaded area in these plots are indicative the higher level of kinetic energy.

in depth the flow evolution in a lid-driven rectangular cavity. We have carried out laminar flow analysis in a rectangular and non-uniform grids. The algebraic equations, thus, are exempt from the necessity of dealing with approximation of metric tensors and employment of turbulence modeling. The predicted physics, thus are contaminated less by numerical errors, and the acquired solution can realistically mimic the flow physics. Based on the problem investigated and the solutions obtained, some important findings from this numerical simulation are summarized below.

1. Beyond $t = 85$, the first two pairs of unsymmetric vortices emerge from where the flow becomes separated. In these counter-rotating vortices, one vortex is not symmetric with the other because they originate from different physical phenomena.
2. Prior to $t = 138$, four pairs of TGL vortices of unsymmetric character have fully developed. Only after the symmetric pair of TGL vortices

is stably formed at $y = 1.5$ does the evolution of the mobile TGL motion enter into a periodic mode having a time-periodicity of 72. In the course of the flow development, which can be classified as periodic, new TGL vortices emerge only at $y \sim 1.7$. Along with unsymmetric TGL vortices moving towards the two end walls, these vortices are destined for immersion into the corner eddies. This implies that the number of TGL vortices does not unconditionally increases. Five pairs, at most, of well-developed TGL vortices are observed in the whole cavity. Subsequent to $t = 138$, three time periods are needed for a pair of TGL vortices, having emerged, to finish their journey.

3. We have discussed the formation of flow instabilities from the energy viewpoint. As the endwall induced left- and right-running vortices spiral monotonically towards the symmetry plane, the normal force exerted there resists the subsequent transport process, leading to the flow destabilization. The isosurface of $v = 0$ is, thus, radially expanded in a direction towards six solid surfaces of the cavity. In the course of this outward extension, a free shear vortex is induced along a curved layer where the kinematic energy takes its local maximum. The formation of shear vortex, in turn, adds an additional drag to the developing boundary layer that is attached to the floor of the cavity, leading to the onset of a wall shear vortex. It is these free- and wall-shear vortices that provide a mechanism for the non-stationary bursting TGL vortices.

References

[1] Burggraf, O. R. (1966). "Analytical and numerical studies of the structure of steady separated flows", *J. Fluid Mech.*, **24**(1), 113–151.

[2] Koseff, J. R. and Street, R. L. (1982). "Visualization studies of a shear driven three-dimensional recirculating flow, Three dimensional Turbulent Shear Driven Flow", *ASME*, 23–31.

[3] Koseff, J. R., Street, R. L., Gresho, P. M., Upson, C. D., Humphrey, J. A. C. and To, W. M. (1983). "A three-dimensional lid-driven cavity flow: experiment and simulation", *in Proc. 3rd Int. Conf. Num. Meth. Lam. and Turb. Flow*, Seattle, August, 564–581.

[4] Rhee, H. S., Koseff, J. R. and Street, R. L. (1984). "Flow visualization of a recirculating flow by rheoscopic liquid and liquid crystal techniques", *Exp. Fluids*, **2**, 57–64.

[5] Koseff, J. R. and Street, R. L. (1984). "Visualization studies of a shear driven three-dimensional recirculating flow", *ASME J. of Fluids Engineering*, **106**(1), 21–29.

[6] Koseff, J. R. and Street, R. L. (1984). "On end wall effects in a lid-driven cavity flow", *ASME J. of Fluids Engineering*, **106**, 385–389.

[7] Koseff, J. R. and Street, R. L. (1984). "The lid-driven cavity flow: A synthesis of qualitative and quantitative observations", *ASME J. of Fluids Engineering*, **106**, 390–398.

[8] Prasad, A. K., Perng, C. Y. and Koseff, J. Y. (1988). "Some observations of the influence of longitudinal vortices in a lid-driven cavity flow", *in Proc. First Nat. Fluid Dynamics Congr.*, Cincinnati, Ohio, 288–295.

[9] Prasad, A. K. and Koseff, J. R. (1989). "Reynolds number and end-wall effects on a lid-driven cavity flow", *Phys. Fluids*, **A1**, 208–218.

[10] Freitas, C. J., Street, R. L., Findikakis, A. N. and Koseff, J. R. (1985). "Numerical simulation of three-dimensional flow in a cavity", *Int. J. Numer. Meths. in Fluids*, **5**, 561–575.

[11] Freitas, C. J. and Street, R. L. (1988). "Non-linear transport phenomena in a complex recirculating flow: A numerical investigation", *Int. J. Numer. Meths. in Fluids*, **8**, 769–802.

[12] Perng, C. Y. and Street, R. L. (1989). "Three-dimensional unsteady flow simulations: alternative strategies for a volume-averaged calculation", *Int. J. Numer. Meths in Fluids*, **9**, 341–362.

[13] Zang, Y., Street, R. L. and Koseff, J. R. (1993). "A dynamic mixed subgrid-scale model and its application to turbulent recirculating flows", *Phys. Fluids*, **A5**(12), 3186–3196.

[14] Aidum, C. K., Triantafillopoulos, N. G. and Benson, J. D. (1991). "Global stability of a lid-driven cavity with throughflow: Flow visualization studies", *Phys. Fluids*, **A3**, 2081–2091.

[15] Deville, M., Lê, T.-H. and Morchoisne, Y. (Eds.) (1992). "Numerical Simulation of 3-D Incompressible Unsteady Viscous Laminar Flows", *Notes on Numerical Fluids Mechanics*, **36**, A GAMM-Workshop.

[16] Deng, G. B., Piquet, J., Queutey, P. and Visonneau, M. (1994). "A new fully coupled solution of the Navier-Stokes equations", *Int. J. Numer. Meths. in Fluids*, **19**, 605–639.

[17] Ladyzhenskaya, O. A. (1963). "Mathematical problems in the dynamics of a viscous incompressible flow," Gordon and Breach, New York.

[18] Leonard, B. P. (1979). "A stable and accurate convective modeling procedure based on quadratic upstream interpolation," *Comput. Methods Appl. Mech. Engrg.*, **19**, 59–98.

[19] Chiang, T. P., Hwang, R. R. and Sheu, W. H. (1996). "Finite volume analysis of spiral motion in a rectangular lid-driven cavity", *Int. J. Numer. Meths. in Fluids*, **23**, 325–346.

[20] Patankar, S. V. (1980). "Numerical Heat Transfer and Fluid Flow", Hemisphere.

[21] Abdallah, S. (1987). "Numerical solution for the incompressible Navier-Stokes equations in primitive variables using a non-staggered grid," II., *J. Comput. Phys.*, **70**, 193–202.

[22] Ethier, C. R. and Steinman, D. A. (1994). "'Exactly fully 3D Navier-Stokes solutions for benchmarking," *Int. J. Numer. Meths. in Fluids*, **19**, 369–375.
[23] Ku, H. C., Hirsh, R. S. and Taylor, T. D. (1987). "A pseudospectral method for solution of the three-dimensional incompressible Navier-Stokes equations", *J. Comput. Phys.*, **70**, 439–462.
[24] Kato, Y., Kawai, H. and Tanahashi, T. (1990). "Numerical flow analysis in a cubic cavity by the GSMAC finite element method," *JSME Int. J. Series II*, **33**(4), 649–658.
[25] Cortes, A. B. and Miller, J. D. (1994). "Numerical experiments with the lid-driven cavity flow problem," *Computer Fluids*, **23**(8), 1005–1027.
[26] Babu, V. and Korpela, S. A. (1994). "Numerical solutions of the incompressible, three-dimensional Navier-Stokes equations", *Computer Fluids*, **23**(5), 675–691.